Full length article

Oncogenic transformation of tubular epithelial ducts: How mechanics affects morphology

D. Ambrosi [a], A. Favata [b] [iD],*, R. Paroni [c], G. Tomassetti [d,e] [iD]

[a] *Department of Mathematical Sciences "G.L. Lagrange", Politecnico di Torino, corso Duca degli Abruzzi 24, Turin, 10129, Italy*
[b] *Department of Structural and Geotechnical Engineering, Sapienza University of Rome, Via Eudossiana 18, Rome, 00184, Italy*
[c] *Department of Civil and Industrial Engineering, University of Pisa, Largo Lucio Lazzarino 1, Pisa, 56122, Italy*
[d] *Department of Industrial, Electronic and Mechanical Engineering, Roma Tre University, Via Vito Volterra 62, Rome, 00146, Italy*
[e] *Istituto per le Applicazioni del Calcolo "Mauro Picone" – CNR, Via dei Taurini 19, Rome, 00185, Italy*

ARTICLE INFO

ABSTRACT

We derive a continuum mechanical model to capture the morphological changes occurring at the pre-tumoral stage of epithelial tissues. The mathematical model, derived from first principles, accounts for the competition between the bulk elasticity of the epithelium and the surface tension of the apical and basal boundaries. The variation of the energy functional yields the Euler–Lagrange equations to be numerically integrated. The numerical results reproduce a variety of morphological shapes, from invagination to evagination, depending on the ratio between bulk and surface energy at variance of the length of the section. In particular, using parameters independently measured, we are able to reproduce experimental data reported for a ring partially made of transformed cells.

1. Introduction

Epithelial tissues are thin, continuous, layers of cells with a small amount of extracellular matrix. In the simplest case there is only a layer of cells (a *monolayer*), connected to each other by molecular forces that provide continuity to the tissue. Epithelial sheets can then undergo a number of active (spontaneous) morphological transitions, orchestrated by the actomyosin machinery, the inner cellular motor able to produce active stress, mostly located at the periphery of the cells (Hannezo et al., 2014; Vicente and Diz-Muñoz, 2023).

In this paper we are interested in epithelial tubular ducts: the tubule is ideally a cylinder, produced by bending a cell monolayer up to closure, when an internal (basal) and an external (apical) surface can be devised. In its healthy state, the section of a tubular duct can therefore be represented as a ring, characterized by a tensional state (a natural curvature) generated by the cortical myosin activity (myosin belt).

The paper by Messal and co-authors (Messal et al., 2019) reports three-dimensional imaging of pancreatic ducts subjected to oncogenic transformation. The images show that the proliferation of malignant cells is associated, at the organ level, with two types of neoplastic morphological changes: exophytic and endophytic. Exophytic transformations involve outward expansion from the duct (evagination), while endophytic transformations manifest as growth inward into the

duct (invagination). Crucially, the lesion morphology is observed to depend on the size of the duct: small-radius samples show exophytic growth, while larger ducts deform endophytically. Such a transition in morphology takes place at a critical size of the duct, thus suggesting that the phenomenon is induced by some characteristic length-scale: since neoplastic transformations are accompanied by overproliferation, one may argue that such scale could be likely be the size of the grown tissue. Numerical simulations based on a three-dimensional vertex model and analysis of an elastic ring model show that the morphology of epithelial tumors is determined by an interplay between geometry and the alteration of the apico-basal tension imbalance induced by cytoskeletal changes. The authors conclude that "*tension imbalance and tissue curvature [are] fundamental determinants of epithelial tumorigenesis*" (Messal et al., 2019). In particular, the intrinsic length-scale that determines the critical size at which the transition is observed from exo- to endo-phytic is the ratio between the bending rigidity (whose physical dimensions are a force times an area) and the active bending moment (force times length) resulting from the difference between apical and basal tension times the width of the monolayer.

The mechanical models of epithelial sheets in the current literature are mostly based on thin shell theory: the aspect ratio of the soft structure enforces the possibility to neglect the thickness of the

---

* Corresponding author.
E-mail addresses: davide.ambrosi@polito.it (D. Ambrosi), antonino.favata@uniroma1.it (A. Favata), roberto.paroni@unipi.it (R. Paroni), giuseppe.tomassetti@uniroma3.it (G. Tomassetti).

tissue (Yin et al., 2021; Borja da Rocha et al., 2022). In a different vein, the imbalance between apical and basal tension as a key factor in epithelial morphology dates back to the pioneering work by Lewis (1947), which emphasizes the critical role of contractile tension in the surface layers of epithelial cells in driving biological invagination. Odell and co-workers (Odell et al., 1981) elaborate this idea proposing a model where epithelial folding is coordinated by propagating waves of cell shape changes induced by contraction at the cell apex due to actin. Similarly Jones and Chapman (2010) propose a continuum model based on thin elastic shell theory with embedded, on one of the sides, a family of contractile fibers. Related works (Krajnc and Ziherl, 2015) confirm that internal tensions within a single-cell-thick epithelial tissue can drive the formation of various morphological states.

While the large literature mentioned above emphasizes the importance of apico-basal tension imbalance as a determining factor in epithelial morphogenesis, the basal side of the epithelium is supported by a basal membrane and by a substrate, the stroma: their combined stiffness can have relevant mechanical effects. Several works focus on the role of the substrate in soft material instabilities such as wrinkling and periodic doubling. As an example, growing rods on an elastic foundation exhibit such instabilities (Almet et al., 2018). In the specific case of epithelial tissues, the recent work in Andrenšek and Krajnc (2025) emphasizes the role of the basal membrane and of the stroma for an initially flat epithelium. All these examples, however, apply to flat films on a substrate: a closed, curved duct is a fundamentally different mechanical system. In particular, the ring's own curvature increases its overall geometric rigidity, which provides a significant restoring force against local buckling. For example, it has been shown in Jia et al. (2018) that intrinsic curvature delays buckling, and hence it is by itself a stabilizing factor. Last, but not least, the morphological changes in inhomogeneous ducts appear to be driven by smooth configurational transitions, rather than instability.

In this paper, we explore the above illustrated morphogenetic mechanism for a quasi-2D duct model: we assume that the organ is long enough to make the study of a transverse section physically significant. The duct section is therefore a slender elastic body, represented as a nonlinear rod with variable cross-section. The aspect ratio of epithelial sheets of our interest can be about 1/20 (Messal et al., 2019): small enough to model the object as a thin structure, but not small enough to neglect strains across the thickness. We study this mechanical system elaborating a mathematical recently developed by some of us (Favata et al., 2022), settled on the large-strain framework and possible thickness distension. This theoretical framework allows us to delve into the transverse thickening of the epithelium that is pivotal in the development of these lesions (Messal et al., 2019).

After the statement of a suitable 2D-averaged kinematics, we assume an energy functional quadratic in the longitudinal strain and linear in the surface strain. Performing its variation, we get the Euler–Lagrange equations that are then numerically integrated. At variance of the total number of cells and imbalance of the surface tension, the results capture a wide spectrum of possible equilibria, a scenario richer than the one predicted in simpler linear frameworks.

2. The mathematical model

We model an epithelial monolayer duct as a closed two-dimensional slender body. Utilizing a kinematic Ansatz drawn from nonlinear rod theories that allow for thickness extension, by a suitable integration we condense the transverse features into a one-dimensional model. The rod is endowed with a bulk and a surface energy on the apical and basal sides. The two energy terms are inherently competing: while the former promotes the retention of the undeformed configuration, the latter prompts bending when there is an imbalance between the apical and basal tensions. The equilibrium configurations are determined by the interplay of the previously mentioned energetic terms and generalizes (Favata et al., 2022,b) by incorporating the initial curvature of the rod.

2.1. Kinematics

We work in two space dimensions, under the assumption of plane strain. Since we are interested in tubular epithelial tissues, we conveniently choose as reference configuration $\mathcal{R}$ a circular strip of thickness h, possibly position-dependent, whose midline is an arc of circumference of length ℓ and radius R, with $h/R \ll 1$. We assume that the ring lies on a plane spanned by two orthonormal vectors e_1 and e_2. We also define $e_3 := e_1 \times e_2$. The material points of the body are labeled using the region

$$\mathcal{B} = \left\{ (x_1, x_2) : x_1 \in (0, \ell), -\frac{h(x_1)}{2} < x_2 < \frac{h(x_1)}{2} \right\}.$$

We parametrize the reference configuration through the mapping $g_0 : \mathcal{B} \to \mathcal{R}$ defined by

$$g_0(x) = r_0(x_1) + x_2 d_0(x_1), \tag{1}$$

where

$$r_0(x_1) = R \cos(x_1/R) e_1 + R \sin(x_1/R) e_2 \quad \text{and} \quad d_0(x_1) = -r_0(x_1)/R,$$

see Fig. 1.

The gradient of g_0 at the point x of $\mathcal{B}$ is

$$\nabla g_0 = \left(1 - \frac{x_2}{R}\right) r_0' \otimes e_1 + d_0 \otimes e_2, \tag{2}$$

since $d_0' = -r_0'/R$. The intermediate configuration $\mathcal{R}$ is introduced for energetic purposes that are discussed below.

We parametrize the deformed configuration $\mathcal{D}$ of the ring through a mapping $g : \mathcal{B} \to \mathcal{D}$ of the form:

$$g(x) = r(x_1) + x_2 d(x_1). \tag{3}$$

The parametric curve $x_1 \mapsto r(x_1)$ describes the deformed configuration of the midline of the ring. The orientation and the norm of $d(x_1)$ define, respectively, the orientation and the stretch of the transversal fiber x_1. To describe a closed regular ring, we assume $r(0) = r(\ell)$, $r'(0) = r'(\ell)$, and $d(0) = d(\ell)$. We require that d be perpendicular to r'. Accordingly, when introducing the local orthonormal basis

$$a_1 = \frac{r'}{|r'|}, \quad \text{and} \quad a_2 = e_3 \times a_1, \tag{4}$$

we can define the midline longitudinal stretch λ and the transversal stretch μ through

$$r' = \lambda a_1, \quad d = \mu a_2. \tag{5}$$

The vector $a_1(x_1)$ uniquely identifies an angle $\vartheta(x_1) \in [0, 2\pi)$ through

$$a_1(x_1) = \cos \vartheta(x_1) e_1 + \sin \vartheta(x_1) e_2. \tag{6}$$

In terms of ϑ, we have $a_2(x_1) = -\sin \vartheta(x_1) e_1 + \cos \vartheta(x_1) e_2$. The gradient of g turns out to be

$$\nabla g = G = (\lambda - x_2 \mu \vartheta') a_1 \otimes e_1 + \mu a_2 \otimes e_2 + x_2 \mu' a_2 \otimes e_1, \tag{7}$$

since $d' = \mu' a_2 - \mu \vartheta' a_1$. The deformation of the ring is the map $f : \mathcal{R} \to \mathcal{D}$ defined by

$$f = g \circ g_0^{-1} : \mathcal{R} \to \mathcal{D}. \tag{8}$$

By (2) and (7), the deformation gradient $F = \nabla f$ at a point $p \in \mathcal{R}$, is

$$F = \nabla g (\nabla g_0)^{-1} = \frac{\lambda - x_2 \mu \vartheta'}{1 - x_2/R} a_1 \otimes r_0' + \frac{x_2 \mu'}{1 - x_2/R} a_2 \otimes r_0' + \mu a_2 \otimes d_0, \tag{9}$$

where ∇g and ∇g_0 are evaluated at $x = g_0^{-1}(p)$.

We next introduce the rotation tensor

$$R = a_1 \otimes r_0' + a_2 \otimes d_0, \tag{10}$$

which maps the reference basis $\{r_0', d_0\}$ onto the current basis $\{a_1, a_2\}$. Since we have in mind to deduce a rod model, we choose as deformation measure

$$D = R^\top F = \frac{\lambda - x_2 \mu \vartheta'}{1 - x_2/R} r_0' \otimes r_0' + \frac{x_2 \mu'}{1 - x_2/R} d_0 \otimes r_0' + \mu d_0 \otimes d_0, \tag{11}$$
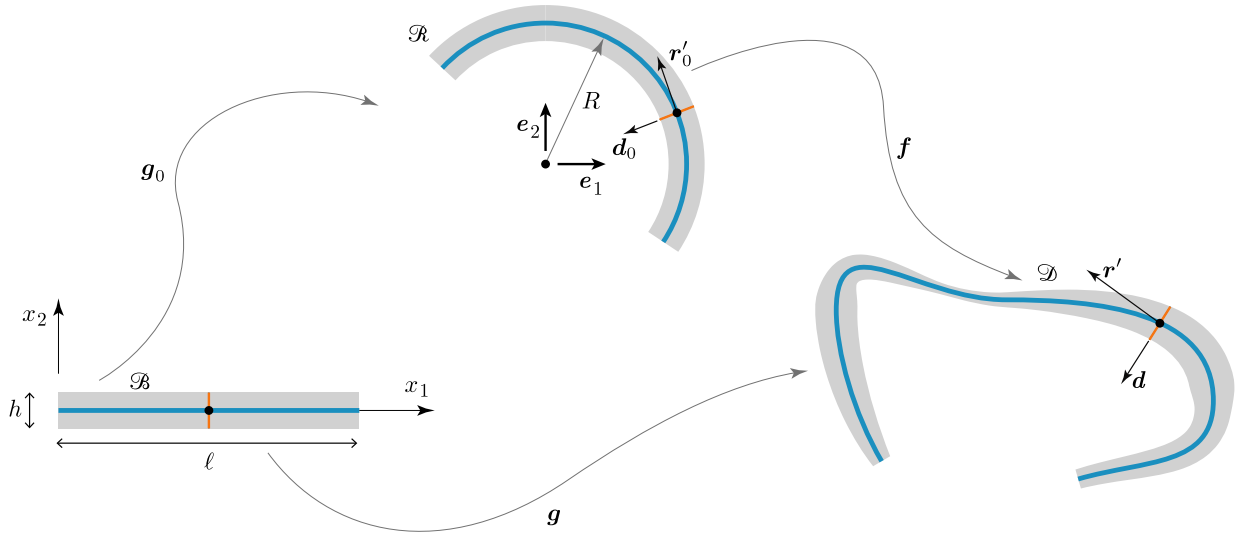
Fig. 1. Geometry of the strip $\mathscr{B}$, the reference configuration $\mathscr{R}$, and the deformed configuration $\mathscr{D}$. For simplicity, the thickness h is depicted as a constant.
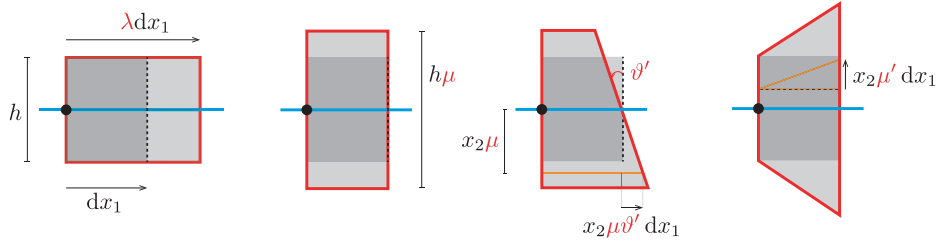

Fig. 2. Cartoon illustrating (from left to right): the average axial stretch, the transverse stretch, the contribution to axial stretch due to the curvature ϑ', and the non-uniform shear deformation due to a non-uniform transverse stretch.

that represents the deformation gradient F free from the rigid rotation of the axis. The first term in Eq. (11) is the sum of two contributions: the *average axial stretch* λ minus the *curvature* of the longitudinal axis ϑ', times the product μx_2, which is the distance from the axis in the *deformed configuration*. Both terms are divided by the Jacobian of g_0, accounting for the curvature of the reference configuration. The second term represents a *non-uniform shear* deformation associated to a possibly non-uniform transverse stretch. The last term on the right-hand side is the *transverse stretch* (see Fig. 2).

While defining $\epsilon = h/R$, we take into account that $|x_2/h| \le 1$ and we have

$$\frac{\lambda - x_2 \mu \vartheta'}{1 - x_2/R} = \frac{R(\lambda/R - \mu \vartheta' x_2/R)}{1 - x_2/R} = R\left(\frac{\lambda}{R} - \mu \vartheta' \frac{x_2}{R}\right)\left(1 + \frac{x_2}{R} + o(\epsilon)\right)$$
$$= R\left(\frac{\lambda}{R} - \mu \vartheta' \frac{x_2}{R} + \frac{x_2 \lambda}{R^2}\right) + o(\epsilon) = \lambda - \left(\mu \vartheta' - \frac{\lambda}{R}\right) x_2 + o(\epsilon)$$

(12)

and

$$\frac{x_2 \mu'}{1 - x_2/R} = x_2 \mu' + o(\epsilon).$$

(13)

Thus, on keeping terms up to order ϵ, we arrive at

$$D \simeq \left(\lambda - (\mu \vartheta' - \lambda \kappa_0) x_2\right) r_0' \otimes r_0' + x_2 \mu' d_0 \otimes r_0' + \mu d_0 \otimes d_0,$$

(14)

where we have set $\kappa_0 = 1/R$.

2.2. Strain energy and active surface tension

In our model, we consider two distinct energetic contributions: a *bulk energy*, due to the mechanical (passive) reaction of the cytoplasm, and a *surface energy*, which incorporates the contractile (active) tension

arising from the network of actin filaments positioned beneath the cell membrane.

Strain energy. We can approximate the strain energy by performing a Taylor expansion up to the second order. This approximation yields:

$$W_b(F) = W_b(D) \simeq \frac{1}{2} D^2 W_b(I)[\text{sym}(D - I), \text{sym}(D - I)].$$

(15)

where D denotes the Fréchet derivative of the energy functional. The approximation (15) assumes that the circular configuration $\mathscr{R}$ ($\lambda = 1$, $\mu = 1$, $\theta' = \kappa_0$) is stress free.

The assumption that the bulk energy is isotropic entails that there exist constants α_1 and α_2 (the Lamé moduli) such that

$$\frac{1}{2} D^2 W_b(I)[\text{sym}(D - I), \text{sym}(D - I)] = \alpha_1 |\text{sym}(D - I)|^2 + \alpha_2 (\text{tr}(D - I))^2.$$

Hereafter, we assume that the two material parameters α_1 and α_2 may vary with x_1, and remain positive and uniformly bounded away from zero. The bulk strain energy per unit length along the direction x_1 is

$$w_b(x_1) = \int_{-h(x_1)/2}^{+h(x_1)/2} W_b(D(x_1, x_2)) dx_2 = \hat{w}_b(\lambda, \mu, \mu', \vartheta'),$$

where

$$\hat{w}_b\left(\lambda, \mu, \mu', \vartheta'\right) = h\left[\alpha_1 \left(\lambda^2 + \mu^2\right) + \alpha_2 (\lambda + \mu)^2 - 2\left(\alpha_1 + 2\alpha_2\right)(\lambda + \mu)\right]$$
$$+ \frac{h^3}{12}\left[\alpha_1 \left(\left(\mu \vartheta' - \lambda \kappa_0\right)^2 + \frac{\mu'^2}{2}\right)\right.$$
$$\left. + \alpha_2 \left(\mu \vartheta' - \lambda \kappa_0\right)^2\right],$$

up to an additive constant.

Surface energy. Most of the actomyosin material is located at the boundary of the cells that form the epithelial duct and it is therefore a

common approach, both in continuum and discrete models, to adopt a surface energy proportional to the length of the boundary (Krajnc et al., 2013; Haas and Goldstein, 2019; Favata et al., 2022,b). We consider a fiber material parallel to e_1. The deformation transforms this fiber into

$$\boldsymbol{G}e_1 = \left(\lambda - x_2 \mu \vartheta'\right) \boldsymbol{a}_1 + x_2 \mu' \boldsymbol{a}_2.$$

Accordingly, the specific elongation of the generic fiber is

$$|\boldsymbol{G}e_1| = \sqrt{\left(\lambda - x_2 \mu \vartheta'\right)^2 + \left(x_2 \mu'\right)^2} = \lambda - x_2 \mu \vartheta' + o(\epsilon). \tag{16}$$

Therefore, discarding terms of order higher than ϵ, we obtain

$$|\boldsymbol{G}e_1| \simeq \lambda - x_2 \mu \vartheta'. \tag{17}$$

The surface energy is taken proportional to the length of the apical and basal fibers, represented as $x_2 = \mp h/2$, respectively. By denoting with σ_a and σ_b the tension of the apical and basal fibers, respectively, Eq. (17) entails the definition of surface energy per unit length in the following manner:

$$w_s\left(\lambda, \mu, \vartheta'\right) = \sigma_a\left(\lambda - \frac{h}{2}\mu\vartheta'\right) + \sigma_b\left(\lambda + \frac{h}{2}\mu\vartheta'\right). \tag{18}$$

We assume that σ_a and σ_b may depend on the length coordinate x_1.

By adding the bulk and surface energies we obtain the total strain energy:

$$\begin{aligned}
\mathcal{E} &= \int_0^\ell \left(w_b(\lambda, \mu, \mu', \vartheta') + w_s(\lambda, \mu, \vartheta')\right) \mathrm{d}x_1 \\
&= \int_0^\ell h\left(\alpha_1\left(\lambda - 1\right)^2 + \alpha_1(\mu - 1)^2 + \alpha_2(\lambda + \mu - 2)^2\right) \mathrm{d}x_1 \\
&\quad + \int_0^\ell \frac{h^3}{12}\left((\alpha_1 + \alpha_2)\left(\mu\vartheta' - \lambda\kappa_0\right)^2 + \alpha_1 \frac{\mu'^2}{2}\right) \mathrm{d}x_1 \\
&\quad + \int_0^\ell \sigma_a\left(\lambda - \frac{h}{2}\mu\vartheta'\right)\mathrm{d}x_1 + \int_0^\ell \sigma_b\left(\lambda + \frac{h}{2}\mu\vartheta'\right)\mathrm{d}x_1.
\end{aligned} \tag{19}$$

In the representation of the energy (19) all the material parameters might in principle depend on the curvilinear coordinate.

Remark 1. The surface contribution in the energy is actually due to the active stress generated by the actomyosin cables at the boundary of the cells. Physically speaking, it is not a strain energy: we are simply using the mathematical formalism to include the active stress as the derivative of a term linear in the stretch. In other words, the surface term is not hyperelastic, there is no energy conservation and its inclusion in the energy for pure mathematical convenience (Ambrosi and Pezzuto, 2012).

Transverse incompressibility. Cells within the epithelial monolayer, which are fluid-filled, exhibit an incompressible nature, as emphasized by previous studies (Krajnc et al., 2013; Haas and Goldstein, 2019). Given that each cell extends across the entire thickness of the layer, it is reasonable to enforce an average incompressibility constraint throughout the thickness:

$$\frac{1}{h(x_1)} \int_{-h(x_1)/2}^{+h(x_1)/2} \det \boldsymbol{F} \, \mathrm{d}x_2 = 1, \tag{20}$$

where

$$\det \boldsymbol{F} = \mu\left(\lambda - (\mu\vartheta' - \lambda\kappa_0)x_2\right). \tag{21}$$

By combining (20) and (21) we obtain:

$$\lambda\mu = 1. \tag{22}$$

Accordingly, we can take ϑ and μ as independent variables for the energy and, using the condition (22), write

$$\begin{aligned}
\mathcal{E} &= \int_0^\ell h\left[\alpha_1\left(\frac{1}{\mu} - 1\right)^2 + \alpha_1(\mu - 1)^2 + \alpha_2\left(\frac{1}{\mu} + \mu - 2\right)^2\right] \mathrm{d}x \\
&\quad + \int_0^\ell \frac{h^3}{12}\left[(\alpha_1 + \alpha_2)\left(\mu\vartheta' - \frac{\kappa_0}{\mu}\right)^2 + \alpha_1 \frac{\mu'^2}{2}\right] \mathrm{d}x \\
&\quad + \int_0^\ell (\sigma_a + \sigma_b)\frac{1}{\mu}\mathrm{d}x + \int_0^\ell \frac{h}{2}(\sigma_b - \sigma_a)\mu\vartheta'\mathrm{d}x,
\end{aligned} \tag{23}$$

up to an additive constant. In the last equation we have set $x = x_1$. We will keep this notation until the end of the paper.

3. Euler equations, interface and boundary conditions

The presence of transformed cells in a ductal epithelium introduces not only inhomogeneities into the problem, but may also cause jump discontinuities in the wall thickness h, the elastic moduli (α_1, α_2), and the surface active tensions (σ_a, σ_b). These discontinuities, in turn, induce jumps in the kinematical variables that describe the system.

Hereafter, we assume h, (α_1, α_2), and (σ_a, σ_b) to be piece-wise smooth. The jump of any quantity will be denoted by $[[\cdot]]$, for instance, the jump of h at $x = s$ is $[[h]](s) = h(s^+) - h(s^-)$.

To account for the jump of material parameters across the wild-transformed interface, it is convenient to write the balance equations in dimensional form. We consider the augmented functional

$$\mathcal{L} = \mathcal{E} - \int_0^\ell \boldsymbol{N} \cdot \left(\boldsymbol{r}' - \frac{1}{\mu}\boldsymbol{a}_1\right) \mathrm{d}x, \tag{24}$$

where $\boldsymbol{N}$ is the Lagrange multiplier that enforces the constraint (5)$_1$. The fields $\boldsymbol{r}$, ϑ, and μ are our kinematically independent variables, that we assume smooth in s.

In our theory, μ, μ', and θ' play the role of strain measures and are indeed invariant under rigid motions. They are related to the position $\boldsymbol{r}$ by the compatibility equationi (24), which we enforce weakly through the Lagrange multiplier $\boldsymbol{N}$. This approach is quite common for Euler's Elastica and for some of its variants, such as thin ribbons (Barsotti et al., 2022; Domokos and Healey, 2005; Moore and Healey, 2019). From a numerical point of view, such a weak enforcement reduces the degree of differentiability required for the solution (see the discussion in Section 5). Furthermore, this weak enforcement has a clear physical implication: it naturally yields the Euler–Lagrange equation $\boldsymbol{N}' = \boldsymbol{0}$, thus identifying the multiplier $\boldsymbol{N}$ with the (constant) internal reaction that preserves compatibility. Alternatively, one may incorporate the constraint directly into the energy functional, by expressing the energy in terms of the unknown $\boldsymbol{r}$, as done in Singh and Hanna (2018). In the present case, however, the assumption of extensible rod would result into an awkward expression with intricate boundary conditions.

We exploit the symmetry of the problem restricting the numerical approximation to half of the rod and we now use the symbol ℓ to denote half the length of the ring. We impose the following essential conditions

$$\boldsymbol{r}(0) = \boldsymbol{0}, \qquad r_x(\ell) = 0, \tag{25a}$$

$$\vartheta(0) = 0, \qquad \vartheta(\ell) = \pi, \tag{25b}$$

$$[[\boldsymbol{r}]] = 0, \qquad [[\vartheta]] = 0, \qquad [[\mu h]] = 0, \tag{25c}$$

where r_x denotes the first component of $\boldsymbol{r}$. The conditions in (25a) prescribe the position of the endpoints of the rod; in particular, the second condition in (25a) follows from the assumed symmetry with respect to the axis $x = 0$. Analogous considerations apply to (25b). The conditions in (25c) enforce the continuity of the position, the smoothness of the midline of the rod, and the continuity of the top and bottom boundaries, respectively.

Performing the first variation of the augmented functional (24), we get the following system of ordinary differential equations, which hold in the regions where all the fields are smooth:

$$\begin{aligned}
&\left[\frac{h^3}{12}\alpha_1\mu'\right]' - 2h\alpha_1\frac{1}{\mu^2}\left(1 - \frac{1}{\mu}\right) \\
&\quad - 2h\alpha_1(\mu - 1) - 2h\alpha_2\left(\frac{1}{\mu} + \mu - 2\right)\left(1 - \frac{1}{\mu^2}\right) \tag{26a} \\
&\quad - \frac{h^3}{6}(\alpha_1 + \alpha_2)\left(\mu\vartheta' - \frac{\kappa_0}{\mu}\right)\left(\vartheta' + \frac{\kappa_0}{\mu^2}\right) + \frac{\sigma_a + \sigma_b}{\mu^2} - \frac{h}{2}(\sigma_b - \sigma_a)\vartheta' \\
&\quad + \frac{N_x}{\mu^2}\cos\vartheta + \frac{N_y}{\mu^2}\sin\vartheta = 0. \tag{26b}
\end{aligned}$$

$$\left[\frac{h^3}{6}(\alpha_1 + \alpha_2)\left(\mu\vartheta' - \frac{\kappa_0}{\mu}\right)\mu\right]' + \left[\frac{h}{2}(\sigma_b - \sigma_a)\mu\right]' + \frac{N_x}{\mu}\sin\vartheta$$

$$- \frac{N_y}{\mu}\cos\vartheta = 0, \tag{26c}$$

$$\boldsymbol{N}' = \boldsymbol{0}, \tag{26d}$$

$$\mu\boldsymbol{r}' = \cos\vartheta\boldsymbol{e}_1 + \sin\vartheta\boldsymbol{e}_2. \tag{26e}$$

where N_x and N_y denote the first and second components of $\boldsymbol{N}$, respectively. Eq. (26a) accounts for the balance of linear momentum in the transverse direction: the elastic strain is balanced by the sum of the surface tension plus two additional terms that involve the longitudinal reactive force. Eq. (26b) is the balance of bending moments, which involves two components, one purely elastic, associated to the bending stiffness and another active one, which is proportional, through the thickness, to the difference between surface tensions. More physical insight is provided in the Appendix, where the equations are discussed in non dimensional form after suitable scaling.

In addition, we obtain three natural conditions and, at the interface, three jump conditions:

$$\left[\left[\frac{h^3}{6}(\alpha_1 + \alpha_2)\mu\left(\mu\vartheta' - \frac{\kappa_0}{\mu}\right) + \frac{h}{2}(\sigma_b - \sigma_a)\mu\right]\right] = 0, \tag{27a}$$

$$\mu'(0) = 0, \quad [[h^3\alpha_1\mu']] = 0, \quad \mu'(\ell) = 0, \tag{27b}$$

$$[[\boldsymbol{N}]] = \boldsymbol{0}, \quad N_y(\ell) = 0. \tag{27c}$$

In summary, in every region where the fields are smooth, the mathematical problem reduces to two pairs of second-order partial differential equations and two pairs of first-order differential equations (26), complemented by the continuity and boundary conditions (25) and (27).

Remark 2. An insight of Eq. (26c) together with the interface condition (27a) reveals the strong analogy between the roles of the natural curvature κ_0 and the apico-basal difference in surface tension: they are both bending couples. In principle κ_0 could be measured independently: the opening angle of a ring of inactive (dead) cells would provide the natural, relaxed, curvature. In practice this information is not available and for very soft matter the mechanical role of κ_0 is expected to be negligible versus the surface tension.

4. Material parameters

Since our main interest is to investigate the role of inhomogeneities in the morphodynamics of the section of a tubular duct, we now consider a ring divided in two portions: one where there are wild-type (healthy) cells and the other composed by transformed (malignant) cells (see Fig. 1).

To maintain a fair degree of generality in our formulation, we allow each part of the duct to have its own material parameters, using the underscores $_w$ and $_t$, to distinguish between wild-type and transformed domains, respectively (see Fig. 3).

Concerning the elastic moduli, the available data across the literature consist of estimates of the Young's modulus. We interpret the available data as referring to wild-type cells, and we list their range in the first row of Table 1. The Young's moduli of wild-type and transformed cells need not coincide; in particular, transformed cells are reported to be softer than their healthy counterparts (see Favata et al. (2022b) and references therein). Accordingly, we introduce the stiffness contrast:

$$K_E = \frac{E_w}{E_t},$$

where E_w and E_t denote the Young's moduli of wild-type and transformed cells, respectively. The range of the stiffness contrast is reported in the second row of Table 1. We make the simplifying assumption that $\nu_t = \nu_w$, and we report their range of values in the third line of Table 1.

Once the values of the Young's moduli and Poisson's ratios for wild-type and transformed cells are assigned, the corresponding Lamé moduli α_1 and α_2 can be written as (see Favata et al. (2022b)):

$$\alpha_1 = \frac{E}{2(1 + \nu)}, \qquad \alpha_2 = \frac{E\nu}{2(1 + \nu)(1 - 2\nu)}. \tag{28}$$

As to the available measurements of surface tension, we interpret them as referring to the apical surface tension of wild-type cells. The range of values from the literature is reported in the last line of Table 1

Basal surface tension in wild-type cells, as well as the apical and basal surface tensions in transformed cells can be estimated on the basis of the experimental measures pMLC2 (phosphorylated Myosin Light Chain) intensity levels (Elliott et al., 2015; Goeckeler and Wysolmerski, 1995) of fluorescence intensity, since surface tension is the result of the contractive activity of the cell cortex, which correlates with pMLC2. Following Clark et al. (2014a), Messal et al. (2019), we assume a proportionality relation between tension and pMLC2:

$$\sigma = \text{pMLC2} \times K_{sp}. \tag{29}$$

for apical and basal surface tension in wild-type and transformed cells. The value of the constant K_{sp} can be obtained from the knowledge of σ_{aw} and pMLC2_{aw}, namely $K_{sp} = \sigma_{aw}/\text{pMLC2}_{aw}$. Values of pMLC2 for apical and basal surface of wild-type and transformed cells are obtained from Messal et al. (2019, Fig 2j), and listed in Table 2.

From the above values we can infer also the other values of σ required in the model, using (29). Results are shown in Table 3.

As in Messal et al. (2019), we assume that wild-type and transformed cells have the same length L. Then the total length ℓ of the monolayer depends on the number of cells $N = N_w + N_t$, where N_w is the number of wild-type cells and N_t is the number of transformed cells, and on L through the relation $\ell = NL$. The reference values are shown in Table 4.

The cell length and height have been inferred from Messal et al. (2019, Fig. 1f). The range for the number N_w of wild-type cells is taken from Messal et al. (2019, Supplementary, Table 1). The number of N_t of transformed cells per cross-section is inferred from the data in Messal et al. (2019, Supplementary material, p. 5), which report total clone sizes at 10 and 21 days after the first transformed cell begins to divide. These numbers are 18 and 57, respectively. Assuming that the cells are arranged in a square lattice covering the duct wall, the number of transformed cells in a cross-sectional ring can be estimated as the square root of this number. This yields approximately $N_t = 4$ and $N_t = 8$ transformed cells per circumferential ring, corresponding, respectively to 10 and 21 days of lesion development. As already observed in Remark 2 the natural curvatures of the wild-type and transformed tissues are not easily measurable. For this reason, we assume $\kappa_{0w} = \kappa_{0t} = 0$.

5. Numerical results

Estimates of the Young's modulus E_w and the apical surface tension σ_{aw} obtained from the literature span wide ranges (see Table 1). This motivates the use of parametric sweeps to explore the influence of these quantities on the equilibrium morphology.

For the problem at hand, since we are studying equilibria, the fundamental dimensions are length and energy. We can therefore perform a change of scale for the corresponding units in such a way that both the Young's modulus and the height of the cells are rescaled to 1. As a result of this change of scale, the numerical value of the surface tension becomes

$$\bar{\sigma}_{aw} = \frac{\sigma_{aw}}{E_w h_w}, \tag{30}$$

where h_w is the reference thickness of the wild-type cells. Consequently, it is sufficient to perform a parametric sweep over $\bar{\sigma}_{aw}$ alone, rather than varying E_w and σ_{aw} independently. For the physical parameters
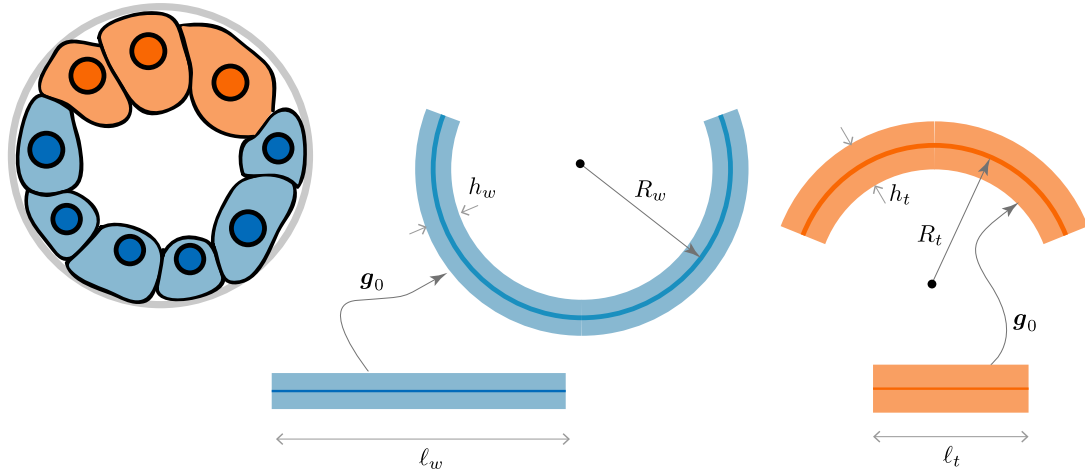
Fig. 3. Left: Cartoon of a duct containing wild-type cells (blue) and transformed cells (orange). Right: geometric representation of the continuum model. (For interpretation of the references to color in this figure legend, the reader is referred to the web version of this article.)

Table 1
Reference values for basic bulk and surface parameters.

Parameter	Symbol	Range	Source
Young's modulus of wild-type cell	E_w	2–100 kPa	Cartagena-Rivera et al. (2017), Song and Janmey (2022)
Stiffness contrast between wild-type and transformed cells	K_E	1–2	Favata et al. (2022b)
Poisson's ratio (wild-type and transformed)	v	0.45–0.49	Roan et al. (2015)
Surface tension apical, wild-type	σ_{aw}	0.1–2.2 nN/μm	Cartagena-Rivera et al. (2017), Clark et al. (2014a)

Table 2
Values of pMLC2 intensity (source (Messal et al., 2019)).

Parameter	Symbol	Range
pMLC2 apical, wild-type	pMLC2$_{a_w}$	2.5–9.0
pMLC2 basal, wild-type	pMLC2$_{b_w}$	0.5–3.5
pMLC2 apical, transformed	pMLC2$_{a_t}$	2.0–5.0
pMLC2 basal, transformed	pMLC2$_{b_t}$	2.0–5.5

Table 3
Derived parameters from Eq. (29).

Parameter	Symbol	Range
Surface tension basal, wild-type	σ_{bw}	0.02–0.8 nN/μm
Surface tension apical, transformed	σ_{at}	0.08–1.1 nN/μm
Surface tension basal, transformed	σ_{bt}	0.08–1.2 nN/μm

Table 4
Geometrical parameters (source (Messal et al., 2019)).

Parameter	Symbol	Values/Range
Cell length (wild-type and transformed)	L	7.0 μm
Cell height, wild-type	h_w	6.2 μm
Ratio between h_t and h_w	K_h	1–1.5
Circumferential number of wild-type cells	N_w	6–50
Circumferential number of transformed cells	N_t	4, 8

that are specified only in a range of values, we adopt the following reference values for the parameters related to

$$v^{\text{ref}} = 0.47, \quad \text{pMLC2}_{aw}^{\text{ref}} = 5.8, \quad \text{pMLC2}_{bw}^{\text{ref}} = 2.0, \quad \text{pMLC2}_{at}^{\text{ref}} = 3.5,$$

$$\text{pMLC2}_{bt}^{\text{ref}} = 3.5. \tag{31}$$

Moreover, we assume, $K_E^{\text{ref}} = 1.0$ and $K_h^{\text{ref}} = 1.0$ as reference values for, respectively, the stiffness contrast and the ratio between h_t and h_w, respectively.

The Euler–Lagrange equations (26) with boundary and interface conditions (25) and (27) are solved numerically in MATLAB using the function bvp4c: equations are rewritten as a system of first order

ODE's and they are numerically solved by a finite difference method implementing shooting to enforce the right endpoint boundary conditions. The convergence of the numerical method is obtained by iteratively increasing the inhomogeneity of the ring, starting from the trivial (circular, homogeneous) case until the desired solution is reached. Since the formulation involves only first derivatives we can use low-order methods. In this particular case we are taking advantage of the fact that the morphological change is not an abrupt transition.

The effect of size. We begin by investigating the role of the number of wild-type cells. To this end, we let the number of wild-type cells N_w vary in the range 10–50, and we explore values of the non-dimensional apical surface tension $\bar{\sigma}_{aw}$ in the range 0.02–0.04. Simulations have been carried out for two representative cases: $N_t = 4$ and $N_t = 8$ transformed cells. The resulting equilibrium configurations are shown in Fig. 4.

The figure shows the theoretically predicted shapes: ducts with smaller diameter remain convex, while ducts with larger diameter exhibit an inward bulging (endophytic growth). The transition to endophytic morphology is observed as N_w becomes larger and as σ_{aw} increases. The results corroborate the hypothesis that the morphology of a lesion within a duct is heavily influenced by the diameter of the duct itself. Fig. 5 shows the detail of the configuration for $N_w = 4$ and $N_t = 8$.

The smaller becomes the duct, the higher the active bending moment required to deform it: this provides an intuitive explanation for the tendency of smaller ducts to remain convex. It is in agreement with the observation, made in the introduction, that the ratio between bending stiffness and active moment provides a length-scale. It is also to be remarked that larger/smaller flexibility are here only of geometrical nature, being related to the length of the rod: it is not necessary to invoke inhomogeneity in the material stiffness and thickness.

These theoretical findings confirm a size-dependent mechanism of morphological regulation in epithelial ducts, potentially relevant in the early detection and characterization of oncogenic transformations in tubular epithelia.

Plots of the angle $\vartheta(x)$ versus the curvilinear coordinate is reported in Fig. 6a, illustrating the induced bending for both $N_t = 4$ and $N_t = 8$
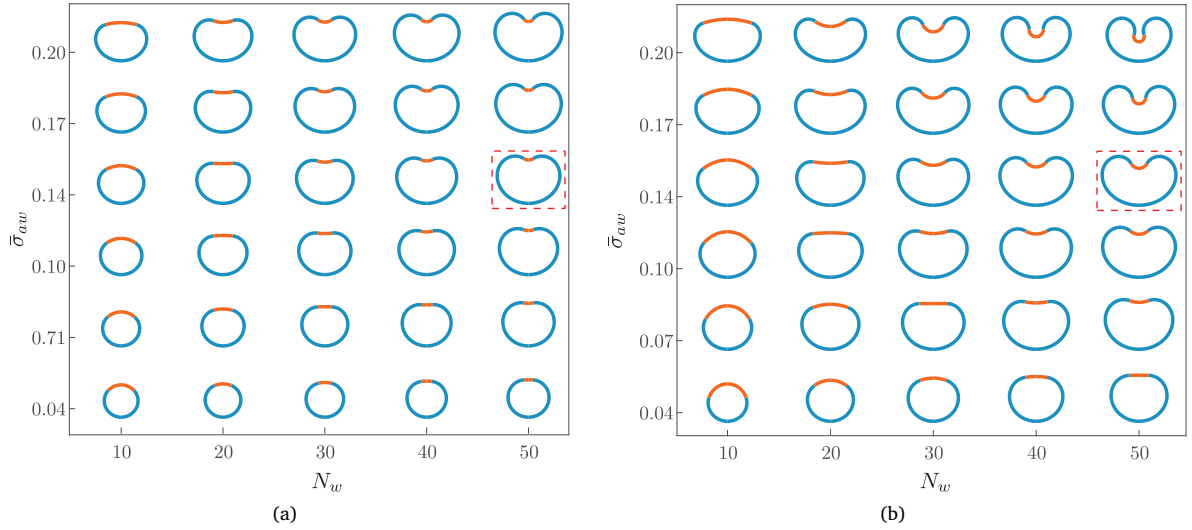
Fig. 4. Equilibrium shapes of the epithelial ring with $N_t = 4$ (left) and $N_t = 8$ (right) transformed cells as a function of the number of wild-type cells (x axis) and the surface tension imbalance parameter (y axis). Each configuration is rescaled by the undeformed ring length so that all shapes are displayed with normalized dimensions. The elements boxed in red are shown in detail in Fig. 5. (For interpretation of the references to color in this figure legend, the reader is referred to the web version of this article.)
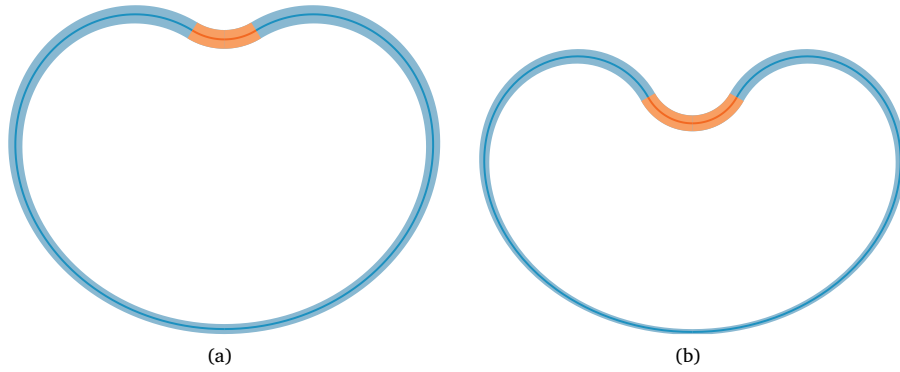
Fig. 5. Morphology of the tubular duct: corresponding to $N_w = 50$ and $\sigma_{aw} = 2.2$ nN/μm of Fig. 4a (left) and Fig. 4b (right). The dashed line is the midline of the rod: in the invagination region the larger bending, the change in curvature and the longitudinal stretch yield a transverse narrowing. For visualization purposes the thickness has been magnified by a scaled factor of 3.

transformed cells. In agreement with the interface conditions (25), (27), the angle ϑ is continuous across the material interface, but its derivative undergoes a jump due the jump surface tension difference. Increasing the number of transformed cells to $N_t = 8$ results in a more pronounced peak for $\vartheta(x)$, indicating a higher bending; this is in agreement with the observed correlation between the size of the transformed region and the induced curvature.

A plot of the transverse stretch $\mu(x)$ is depicted in Fig. 6b for $N_t = 4$ and $N_t = 8$ transformed cells. We observe that thickness changes can be of considerable extent especially in the transformed region. Based on experience with large-strain structural theories for soft materials (Lucantonio et al., 2017; Rubin and Tomassetti, 2025) (see in particular the discussion in Rubin and Tomassetti (2025, Sec. 5.3.4)) we argue that since the material is almost incompressible, a simpler theory without thickness extension would result in a limitation of axial extension, and in turn into an overestimate of the extensional stiffness of the tissue.

It is also interesting to observe that the curvatures in the two regions (wild-type and transformed) which are given by the slopes of the graphs of $\vartheta(x)$, are essentially constant. On the other hand, the corresponding curves are not circles because the axial stretch $\lambda = 1/\mu$ is not constant.

The effect of heterogeneity. To assess the role of mechanical heterogeneity between wild-type and transformed regions, we let the apical and basal pMLC2 levels of the transformed region, denoted below by pMLC2$_{a/bt}$, depend on a *transformation parameter* δ through

$$\text{pMLC2}_{a/bt}(\delta) = \text{pMLC2}_{a/bw}^{\text{ref}} + \delta\left(\text{pMLC2}_{a/bt}^{\text{ref}} - \text{pMLC2}_{a/bw}^{\text{ref}}\right), \qquad (32)$$

where pMLC2$_{a/b}^{w,\text{ref}}$ are the reference values of the apical and basal pMLC2 levels in wild-type cells, and pMLC2$_{a/b}^{t,\text{ref}}$ are the corresponding reference values for fully transformed cells. The transformation parameter δ modulates the contrast between mechanical properties of the two regions. In particular, for $\delta = 0$ the epithelium is mechanically homogeneous, while for $\delta = 1$ it exhibits maximum heterogeneity. In our simulations, we observed that values of δ smaller than 0.4 result in very small deviations from the circular shape. Therefore, we only show the results of our computations in the range $\delta \in [0.4, 1]$. As in previous figures, the non-dimensional apical surface tension $\bar{\sigma}_{aw}$ defined in (30) is varied in the range 0.04–0.2. The number of wild-type and transformed cells are taken, respectively, as $N_w = 30$ and $N_t = 6$.

The following observations can be made. First, for low values of δ the tissue is nearly homogeneous, and the ring remains close to circular,
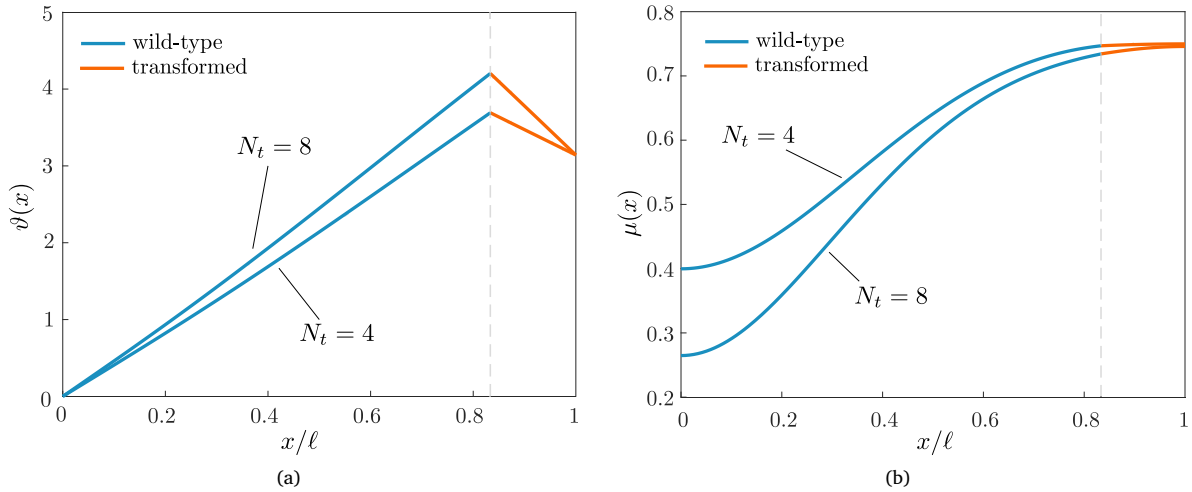
Fig. 6. Rotation ϑ and thickness stretch μ for $N_t = 4$ (thin lines) and $N_t = 8$ (thick lines). Solid lines correspond to the wild-type region and dashed lines to the transformed region.
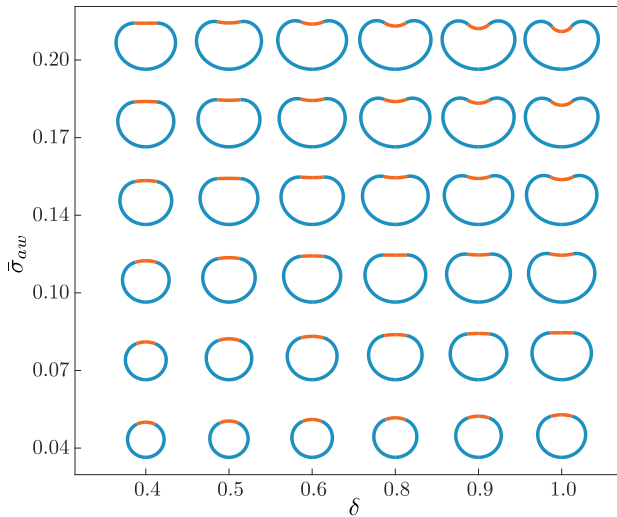
Fig. 7. Effect of the inhomogeneity, as measured by the transformation parameter δ in (32).

even at higher surface tension. As δ increases, the mechanical heterogeneity becomes more pronounced, and the ring exhibits increasing deformation, especially at higher $\bar{\sigma}_{aw}$. The transition from convex to non-convex morphologies becomes evident as both parameters increase (see Fig. 7).

6. Final remarks

In this paper we have investigated the role of mechanical inhomogeneities in determining the morphology of a partially transformed epithelial duct. We have specifically addressed the role of the imbalance between apical and basal surface tension and the tensional difference that characterizes healthy versus tumor cells. The difference in cortical tension generates a torque that can be effectively represented in a mathematical model of a rod enriched with a degree of freedom in the transverse thickness, that has been derived in detail.

The mathematical model rewrites as a couple of nonlinear second order ordinary differential equations (in strain and curvature) with boundary and interface conditions. The equations have been numerically integrated and the results are discussed running the code with

physical parameters set in the range evinced from the biophysical literature.

The numerical simulations reproduce the experimental evidence that the lesion morphology is strongly related to size (the number of cells), with large ducts developing invagination, as opposed to small ducts. The amount of strain which emerges from these simulations confirms the necessity of employing a model that accounts for thickness change, in order not to overestimate the stiffness of the tissue. Our results also show that the known inhomogeneity in surface tension that characterizes lesions is in itself sufficient to generate morphodynamics.

CRediT authorship contribution statement

D. Ambrosi: Writing – review & editing, Writing – original draft, Methodology, Investigation, Formal analysis, Conceptualization. **A. Favata:** Writing – review & editing, Writing – original draft, Methodology, Investigation, Formal analysis, Conceptualization. **R. Paroni:** Writing – review & editing, Writing – original draft, Methodology, Investigation, Formal analysis, Conceptualization. **G. Tomassetti:** Writing – review & editing, Writing – original draft, Methodology, Investigation, Formal analysis, Conceptualization.

Declaration of competing interest

The authors declare that they have no known competing financial interests or personal relationships that could have appeared to influence the work reported in this paper.

Acknowledgments

Appendix. Non-dimensional analysis

Although we have found it convenient to work with dimensional quantities, in this appendix we propose a non-dimensionalized version of the energy functional and the resulting Euler–Lagrange equations. The goal is to make the relevant parameters in the physics of the problem more transparent. We assume that all the physical parameters in (23) are constant and do not depend on the curvilinear coordinate (the case when material parameters are piecewise-constant can be handled by considering separate problems for each part of the epithelial tissue, combined through appropriate continuity/jump conditions). We are therefore allowed to introduce the following dimensionless numbers:

$$\varepsilon = \frac{h}{\ell}, \quad \bar{\sigma}_a = \frac{\sigma_a}{Eh}, \quad \bar{\sigma}_b = \frac{\sigma_b}{Eh}, \quad \sigma = \frac{\bar{\sigma}_a + \bar{\sigma}_b}{2}, \quad \gamma = \frac{\bar{\sigma}_b - \bar{\sigma}_a}{2}\frac{\ell}{h}. \quad (33)$$

The dimensionless quantity $\varepsilon = h/\ell \ll 1$ measures the slenderness of the rod. The parameters $\bar{\sigma}_a$ and $\bar{\sigma}_b$ are the apical and basal surface tensions normalized with respect to the characteristic longitudinal elastic stiffness per unit width Eh. Their arithmetic mean σ provides an effective measure of the average active tension acting on the apical and basal surfaces. The parameter γ quantifies the imbalance between basal and apical normalized tensions, amplified by the geometric factor ℓ/h. In particular, $\gamma = 0$ corresponds to a perfectly balanced distribution of surface tensions, whereas large values of $|\gamma|$ indicate a pronounced asymmetry, which can generate significant bending moments even when $\bar{\sigma}_a$ and $\bar{\sigma}_b$ are individually small.

Rescaling the longitudinal coordinate with ℓ, and using the definitions (28), the total energy can be written in non-dimensional form:

$$\frac{2(1+\nu)}{E\ell^2}\mathscr{E} = \varepsilon \int_0^1 \left[\left(\frac{1}{\mu} - 1\right)^2 + (\mu - 1)^2 + \frac{\nu}{1 - 2\nu}\left(\frac{1}{\mu} + \mu - 2\right)^2 \right] dx$$
$$+ \frac{\varepsilon^3}{12}\int_0^1 \left[\frac{1+\nu}{1+2\nu}\left(\mu\vartheta' - \frac{\kappa_0}{\mu}\right)^2 + \frac{\mu'^2}{2} \right] dx$$
$$+ \varepsilon(1+\nu)\sigma \int_0^1 \frac{1}{\mu}dx + 2\varepsilon^3(1+\nu)\gamma \int_0^1 \mu\vartheta' dx. \quad (34)$$

With a slight abuse of notation, we retain the same symbols for the dimensionless quantities, which are the only ones considered in this section. Inspection of Eq. (34) clarifies the rationale for the distinguished scaling (33): both the strain energy and the total surface energy scale as ε, whereas the bending energy scales as ε^3, mirroring the scaling of the surface–tension difference.

The first variation of the energy functional with respect to μ leads to

$$\varepsilon^3 \left[\frac{\mu''}{12} - \frac{1+\nu}{6(1+2\nu)}\left(\mu\vartheta' - \frac{\kappa_0}{\mu}\right)\left(\vartheta' + \frac{\kappa_0}{\mu^2}\right) - 2(1+\nu)\gamma\vartheta' \right]$$
$$- \varepsilon \left[2\frac{\mu^2 - 1}{1 - 2\nu}\left(\frac{1-\nu}{\mu^3} + \frac{1}{\mu^2} + \frac{1-\nu}{\mu}\right) - (1+\nu)\frac{\sigma}{\mu^2} \right] = 0, \quad (35)$$

while the variation with respect to ϑ gives

$$\left[\frac{1}{12}\left(\mu\vartheta' - \frac{\kappa_0}{\mu}\right)\mu + (1+2\nu)\gamma\mu \right]' = 0. \quad (36)$$

Eq. (35) reveals the competition between bending and stretching, as indicated by the two groups of terms scaling with ε^3 and ε, respectively. In particular, the last of the terms scaling with ε represents the active surface tension that tends to stretch the rod; it is proportional to the normalized mean surface tension σ. The second term scaling with ε^3 accounts for the coupling between bending and transverse stretching, independently of σ. We also observe that the curvature of the rod enhances the transverse stretch when $\vartheta' > \kappa_0/\mu^2$, whereas it reduces it when $\vartheta' < \kappa_0/\mu^2$. We interpret this behavior as a variant of the Brazier effect (Antman, 1973, 2005; Podio-Guidugli, 1982).

Eq. (36) represents a moment balance and does not exhibit distinct scalings in ε. Indeed, the term enclosed in square brackets corresponds

to the normalized effective bending moment, which must remain constant. It consists of two contributions: a bulk term, reflecting the coupled effect of transverse stretching μ and local curvature ϑ'; if the rod were unable to change its thickness, this term would reduce to a moment proportional to $\vartheta' - \kappa_0$, as expected in classical rod theories. The second contribution is an active moment, proportional to the imbalance γ between the normalized apical and basal surface tensions.

It is also worth noting that, if we keep only terms up to first order in ε, Eq. (35) reduces to

$$2\frac{\mu^2 - 1}{1 - 2\nu}\left(\frac{1-\nu}{\mu^3} + \frac{1}{\mu^2} + \frac{1-\nu}{\mu}\right) - (1+\nu)\frac{\sigma}{\mu^2} = 0, \quad (37)$$

which describes a balance between strain and surface tension, entirely decoupled from bending. Any continuous solution $\mu(s)$ of (37) must be constant (in particular, $\mu(s) = 1$ is a solution for $\sigma = 0$). For these solutions, (36) reduces to $\vartheta'' = 0$, that is, the rod has constant curvature. In this latter case, the effect of the surface-tension imbalance, measured by the parameter γ is only through the boundary conditions.

Data availability

No data was used for the research described in the article.

References

Almet, A.A., Byrne, H.M., Maini, P.K., Moulton, D.E., 2018. Post-buckling behaviour of a growing elastic rod. J. Math. Biol. 78, 777–814.

Ambrosi, D., Pezzuto, S., 2012. Active stress vs. active strain in mechanobiology: constitutive issues. J. Elasticity 107 (2), 199–212.

Andrenšek, U., Krajnc, M., 2025. Emergent epithelial elasticity governed by interfacial surface mechanics and substrate interaction. arXiv preprint arXiv:2504.15673.

Antman, S.S., 1973. The theory of rods. In: Truesdell, C. (Ed.), Linear Theories of Elasticity and Thermoelasticity. Springer, Berlin.

Antman, S.S., 2005. Nonlinear Problems of Elasticity. Springer, New York.

Barsotti, R., Paroni, R., Tomassetti, G., 2022. On the stability of the helicoidal configuration in ribbons subjected to combined traction and twist. Int. J. Solids Struct. 250, 111692.

Borja da Rocha, H., Bleyer, J., Turlier, H., 2022. A viscous active shell theory of the cell cortex. J. Mech. Phys. Solids 164, 104876.

Cartagena-Rivera, A.X., Van Itallie, C.M., Anderson, J.M., Chadwick, R.S., 2017. Apical surface supracellular mechanical properties in polarized epithelium using noninvasive acoustic force spectroscopy. Nat. Commun. 8 (1), 1030.

Clark, A.G., Wartlick, O., Salbreux, G., Paluch, E.K., 2014a. Stresses at the cell surface during animal cell morphogenesis. Curr. Biology 24 (8), R484–R494.

Domokos, G., Healey, T.J., 2005. Multiple helical perversions of finite, intrinsically curved rods. Int. J. Bifurc. Chaos 15 (3), 871–890.

Elliott, H., Fischer, R.S., Myers, K.A., Desai, R.A., Gao, L., Chen, C.S., Adelstein, R.S., Waterman, C.M., Danuser, G., 2015. Myosin II controls cellular branching morphogenesis and migration in three dimensions by minimizing cell–surface curvature. Nature Cell Biol. 17 (2), 137–147.

Favata, A., Paroni, R., Recrosi, F., Tomassetti, G., 2022. Competition between epithelial tissue elasticity and surface tension in cancer morphogenesis. Internat. J. Engrg. Sci. 176, 103677.

Favata, A., Paroni, R., Recrosi, F., Tomassetti, G., 2022b. Young modulus of healthy and cancerous epithelial tissues from indirect measurements. Mech. Res. Commun. 124, 103952.

Goeckeler, Z.M., Wysolmerski, R.B., 1995. Myosin light chain kinase-regulated endothelial cell contraction: the relationship between isometric tension, actin polymerization, and myosin phosphorylation. J. Cell. Biol. 130 (3), 613–627.

Haas, P.A., Goldstein, R.E., 2019. Nonlinear and nonlocal elasticity in coarse-grained differential-tension models of epithelia. Phys. Rev. E 99, 022411.

Hannezo, E., Prost, J., Joanny, J.F., 2014. Theory of epithelial sheet morphology in three dimensions. Proc. Natl. Acad. Sci. USA 111, 27–32.

Jia, F., Pearce, S.P., Goriely, A., 2018. Curvature delays growth-induced wrinkling. Phys. Rev. E 98 (3), 033003.

Jones, G.W., Chapman, S.J., 2010. Modelling apical constriction in epithelia using elastic shell theory. Biomech. Model. Mechanobiol. 9 (3), 247–261.

Krajnc, M., Štorgel, N., Hočevar Brezavšček, A., Ziherl, P., 2013. A tension-based model of flat and corrugated simple epithelia. Soft Matter 9, 5323–5330.

Krajnc, M., Ziherl, P., 2015. Theory of epithelial elasticity. Phys. Rev. E 92, 052713.

Lewis, W.H., 1947. Mechanics of invagination. Anat. Rec. 97 (2), 139–156.

Lucantonio, A., Tomassetti, G., DeSimone, A., 2017. Large-strain poroelastic plate theory for polymer gels with applications to swelling-induced morphing of composite plates. Compos. Part B: Eng. 115, 330–340.

Messal, H.A., Alt, S., Ferreira, R.M.M., Gribben, C., Wang, V.M.-Y., Cotoi, C.G., Salbreux, G., Behrens, A., 2019. Tissue curvature and apicobasal mechanical tension imbalance instruct cancer morphogenesis. Nature 566, 126–130.

Moore, A., Healey, T.J., 2019. Computation of elastic equilibria of complete Möbius bands and their stability. Math. Mech. Solids 24 (4), 939–967.

Odell, G.M., Oster, G., Alberch, P., Burnside, B., 1981. The mechanical basis of morphogenesis. I. Epithelial folding and invagination. Dev. Biol. 85 (2), 446–462.

Podio-Guidugli, P., 1982. Flexural instabilities of elastic rods. J. Elasticity 12 (1), 3–17.

Roan, E., Wilhelm, K.R., Waters, C.M., 2015. Kymographic imaging of the elastic modulus of epithelial cells during the onset of migration. Biophys. J. 109 (10), 2051–2057.

Rubin, M.B., Tomassetti, G., 2025. An Eulerian formulation of a constrained variable thickness growing cosserat shell. Int. J. Solids Struct. 316, 113364.

Singh, H., Hanna, J.A., 2018. On the planar elastica, stress, and material stress. J. Elasticity 133 (2), 175–188.

Song, D., Janmey, P., 2022. Watching a cell sheet transforming from soft to stiff. Biophys. J. 121 (8), 1349–1351.

Vicente, F.N., Diz-Muñoz, A., 2023. Order from chaos: how mechanics shape epithelia and promote self-organization. Curr. Opin. Syst. Biology 32–33, 100446.

Yin, S., Li, B., Feng, X.Q., 2021. Bio-chemo-mechanical theory of active shells. J. Mech. Phys. Solids 152, 104419.